CrossMark

Outward Migration of Super-Jupiters

Adam M. Dempsey[1] ⬥, Diego J. Muñoz[2,3] ⬥, and Yoram Lithwick[2] ⬥

[1] Theoretical Division, Los Alamos National Laboratory, Los Alamos, NM 87545, USA; adempsey@lanl.gov

[2] Center for Interdisciplinary Exploration and Research in Astrophysics (CIERA) and Department of Physics and Astronomy, Northwestern University, 2145 Sheridan Road, Evanston, IL 60208, USA

[3] Facultad de Ingeniería y Ciencias, Universidad Adolfo Ibáñez, Av. Diagonal las Torres 2640, Peñalolén, Santiago, Chile

Abstract

Recent simulations show that giant planets of about 1 M_J migrate inward at a rate that differs from the type II prediction. Here we show that at higher masses, planets migrate outward. Our result differs from previous ones because of our longer simulation times, lower viscosity, and boundary conditions that allow the disk to reach a viscous steady state. We show that, for planets on circular orbits, the transition from inward to outward migration coincides with the known transition from circular to eccentric disks that occurs for planets more massive than a few Jupiters. In an eccentric disk, the torque on the outer disk weakens due to two effects: the planet launches weaker waves, and those waves travel further before damping. As a result, the torque on the inner disk dominates, and the planet pushes itself outward. Our results suggest that the many super-Jupiters observed by direct imaging at large distances from the star may have gotten there by outward migration.

Unified Astronomy Thesaurus concepts: Protoplanetary disks (1300); Planetary migration (2206); Planet formation (1241)

1. Introduction

It has long been thought that gap-opening planets migrate by type II migration (Ward 1997; Armitage 2010; Kley & Nelson 2012). In type II, it is hypothesized that planets open gaps that are empty of gas. As a result, gas does not cross a planet's orbit, and the planet is forced to migrate in lockstep with the disk's inward accretion flow. But this hypothesis is at odds with hydrodynamical simulations, which find that inward gas flow is largely unimpeded by a deep gap (Lubow et al. 1999; Crida et al. 2006; Duffell et al. 2014; Fung et al. 2014; Dürmann & Kley 2015; Kanagawa et al. 2017; Robert et al. 2018). Furthermore, recent simulations show that the migration rate of Jupiter-mass planets differs from the type II prediction (Dürmann & Kley 2015; Kanagawa et al. 2018; Dempsey et al. 2020a, hereafter DLL). And as shown in Figure 12 of DLL, the rates found by different groups agree with each other. Theoretically, the reason for the failure of type II is understood (see Section 1.1).

But the question of what happens for planets more massive than Jupiter has not been adequately addressed. One might expect that sufficiently massive planets clear deep enough gaps to satisfy the criterion of type II migration. However, once a planet's mass exceeds around twice that of Jupiter, it excites the disk's eccentricity (Kley & Dirksen 2006; Regály et al. 2010; Teyssandier & Ogilvie 2016, 2017), and the eccentricity of the gas will affect how the planet is torqued. This effect has not been explored in viscous steady state, and the resulting long-term migration rate is thus poorly constrained.

A change in migration direction should occur for very massive secondaries, since it is now known that binary stars of near-equal mass ratio expand while embedded in a disk (Muñoz et al. 2019, 2020; Moody et al. 2019; Duffell et al. 2020). Indeed, such a transition was found by Duffell et al. (2020) to occur in the brown dwarf regime, albeit using viscosities and scale heights larger than are typically expected in protoplanetary disks. In this paper, we show that the migration transition depends on viscosity and scale height, and

that in more realistic disks, the transitional companion mass is around twice the mass of Jupiter. This transition coincides with the development of substantial eccentricity in the disk.

1.1. Theory: Beyond Type II

A planet embedded in a disk excites waves (Goldreich & Tremaine 1979). These waves carry angular momentum and therefore torque the disk where they damp, thereby altering the disk's surface density profile. Furthermore, the waves' angular momentum comes at the expense of the planet's, and so the planet must migrate. Goldreich & Tremaine (1980), Artymowicz (1993), and Ward (1997) worked out how much angular momentum is excited in waves, and their theory adequately predicts what is found in simulations, even for very deep gaps and Jupiter-mass planets—provided the surface density profile is known (see, e.g., the comparison in Figure 14 of DLL).

There is, however, an important missing component: how far do waves travel before damping? The answer is crucial, because even if the waves' angular momentum is known, one can only determine how the waves affect the disk's (azimuthally averaged) surface density profile if one knows where that angular momentum is deposited. The surface density profile, in turn, determines the amplitude of the excited waves, and hence the angular momentum carried by them. Ward (1997) answered this question by assuming that waves damp immediately upon being excited. With this assumption, gaps are exponentially deep for planet masses slightly greater than the gap-opening threshold (Syer & Clarke 1995; Ward 1997). Therefore, disk material is strongly prevented from crossing the planet's orbit, and the planet is locked in the disk—aka the type II paradigm.

The assumption of zero damping length is unfounded, as recognized by Ward (1997, Section IV-b) and many others (e.g., Lunine & Stevenson 1982; Goodman & Rafikov 2001; Rafikov 2002; Duffell 2015; Kanagawa et al. 2015). If the waves travel before damping, the predicted gap becomes much shallower than the exponential depth at zero damping length

(Crida et al. 2006; Duffell 2015; Kanagawa et al. 2015; Ginzburg & Sari 2018; DLL). This is true even if the damping length is modest—of order a scale height. The fact that simulated gaps are not exponentially deep, and the reason for the failure of type II, is therefore simply that waves travel before damping.[4] In order to accurately determine where in the disk the waves damp, and thereby obtain the gap depth and the torques on the planets, one may build a theory, as has been done for low-mass planets (e.g., Goodman & Rafikov 2001). But for near-Jupiter-mass planets, which excite strongly nonlinear waves, the theory has thus far proven intractable. Therefore, we turn to hydrodynamical simulations.

2. Simulations

We run 2D hydrodynamical simulations that are very similar to those in DLL. But we focus now on super-Jupiters. The disk is fed at large radii with constant mass flux ($\dot{M}$) and is evolved long enough that it reaches a viscous steady state. The planet is fixed on a circular orbit with radius r_p and orbital frequency Ω_p. We assume that the disk has a sufficiently low mass that it is appropriate to treat the planet's orbit as fixed when finding the disk's steady-state structure. As shown in Section 4, that assumption restricts the disk's mass to being less than the planet's.

We use the staggered-mesh GPU-accelerated code FAR-GO3D (Benítez-Llambay & Masset 2016). The disk feels the gravity of both planet and star, as well as pressure and viscosity. The disk is locally isothermal with sound speed $c_s = h\Omega r$, where h is the spatially constant disk aspect ratio, r is distance to the star, and Ω is the Keplerian orbital frequency. We adopt the Shakura & Sunyaev (1973) α-viscosity model, setting the kinematic shear viscosity to $\nu = \alpha c_s^2/\Omega$ with a spatially constant α.

The code is run in the frame centered on the star and corotating with the planet. We therefore include the indirect potential due to the acceleration of the star by the planet. Further details regarding the indirect potential are in Appendix A.

We divide the mesh into nearly square cells, with dimensions $\Delta \ln r = \Delta \phi = \text{constant}$ throughout the domain. For the bulk of our simulations, we use a resolution of eight cells per scale height. In Appendix C (Figure 5), we show with an example simulation that this grid size is adequate for determining the total torque injected by the planet.

The principal result of each simulation is the torque on the disk in steady state, ΔT, which is the sum of the (positive) torque on the outer disk and the (negative) torque on the inner disk:

$$\Delta T = -\int_{\text{disk}} \Sigma \frac{\partial \Phi_p}{\partial \phi} r dr d\phi, \quad (1)$$

where Φ_p is the planet's gravitational potential, and Σ is the gas surface density. The normalized torque is $\Delta T/(\dot{M}\ell_p)$, where $\ell_p = r_p^2 \Omega_p$. It is a function only of our three basic parameters,

α, h, and the planet–star mass ratio (q); in particular, it is independent of $\dot{M}$ and hence of disk mass.

2.1. Boundary Conditions

The main difference between the simulations in DLL and those done by other groups is the boundary conditions. Conventionally, the disk is fixed to its initial profile at the boundaries. But that does not allow the disk to relax to a steady-state profile that is independent of the boundary locations. Instead, at our outer boundary, the disk is fed with a constant $\dot{M}$ by using the analytic solution for a steady-state disk beyond the zone where the waves have damped. That solution permits a pileup or deficit of gas beyond the planet's orbit. And at the inner boundary, material is drained without injecting angular momentum, which allows the disk there to reach the surface density profile of a free steady disk, which has $\dot{M} = 3\pi\nu\Sigma$. In practice, this is done by setting $\nu\Sigma$ to be constant across the inner boundary (see also the discussion of the inner boundary condition in Dempsey et al. 2020b). Our boundary conditions are valid whether or not the type II hypothesis is correct. If it is correct, i.e., if no material crosses the planet's orbit, then the inner disk in our simulations would drain away, and the outer pileup would continually grow. Instead, we find that the disk reaches a viscous steady state, with a constant flow past the planet.

Our boundary conditions here differ from DLL in one significant way: we enforce the outer boundary condition in the barycentric frame (see Appendix B for details). If we instead use the stellocentric frame, we find that the indirect terms generate an artificial eccentricity near the outer boundary—an effect that was less pronounced in DLL because of the smaller-mass planets considered there. In many of these new simulations, the disks are found to be eccentric. But in all cases, the eccentricity near the outer boundary is sufficiently small that it is appropriate to treat orbits there as circular around the barycenter (e.g., Figure 3 below).

For most of our simulations, we place the computational boundaries at $r_{\text{in}} = 0.3 r_p$ and $r_{\text{out}} = 12 r_p$, where r_p is the planet's orbital radius. To prevent wave reflections near the inner boundary, we place a wave-killing region between $r = [0.3 r_p, 0.4 r_p]$.[5] Our method of wave killing preserves angular momentum (DLL) and so captures all of the torque injected by the planet in the computational domain. Wave killing is unnecessary at the distant outer boundary, because waves dissipate before reaching it.

3. Results

3.1. Planet Migration and Disk Eccentricity

We run simulations with the q, α, and h values shown in Figure 1. Each simulation is run until the time- and azimuthally averaged $\dot{M}(r)$ profile is spatially constant to within $<10\%$ (see Appendix C). In many of the simulations, ΔT does not reach a constant but instead varies quasiperiodically in a steady state (see Figure 5). As discussed below, the quasiperiodicity is associated with the disk being eccentric and apsidally precessing.

---

[4] Scardoni et al. (2020) presented simulation results in which planets migrate close to the predicted type II rate after transients have died away. They therefore claimed that type II is correct. But their final migration rates are only close to the predicted value—and, in fact, are in agreement with the prior simulation results that show a clear difference from type II (Dürmann & Kley 2015; Kanagawa et al. 2018; DLL; Kanagawa & Tanaka 2020). More tellingly, they plotted the mass flow through the gap and found that it does not vanish, in contradiction with the basic postulate of type II.

---

[5] Our simulations with the highest h have a smaller inner boundary, $r_{\text{in}} = 0.1 r_p$, and wave killing up to $r = 0.2 r_p$, because wave deposition extends further at high h.
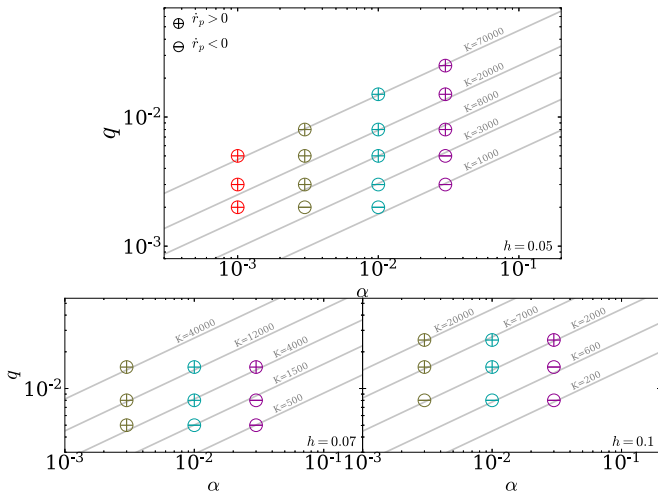
Figure 1. Parameters covered by our simulations. We denote the resulting direction of planet migration with a plus sign for outward migration and a minus sign for inward. Diagonal lines have constant $K = q^2/(\alpha h^5)$.

Convergence typically takes up to seven viscous times, evaluated at r_p. The simulations are computationally expensive both because we run for a number of viscous times and because some disks become eccentric, which forces the time step to be smaller. For example, on a single P100 GPU, one viscous time at r_p takes ~20 days of wall time for our lowest α simulations.

In Figure 1, we plot a plus or minus sign to indicate the direction of the planet's migration. At each h, the transition between inward and outward migration is roughly determined by the value of $K \equiv q^2/(\alpha h^5)$, with the critical value of K depending on h. We note that K is equal to the ratio of the one-sided torque in the absence of a gap ($\propto q^2/h^3$) to the viscous torque ($\propto \alpha h^2$; Lin & Papaloizou 1986; Duffell & MacFadyen 2013; Kanagawa et al. 2015) and found in simulations to set the gap depth when $q \lesssim 10^{-3}$ (Duffell & MacFadyen 2013; Fung et al. 2014; Kanagawa et al. 2017).

The migration rate is obtained by angular momentum conservation, $\frac{1}{2}M_p \ell_p \dot{r}_p / r_p = -\Delta T$, where M_p is planet mass. We may rewrite this as

$$\frac{\dot{r}_p}{r_p} = -\frac{1}{\tau_\nu^*}\left(\frac{\Delta T}{\dot{M}\ell_p}\right), \qquad (2)$$

where

$$\frac{1}{\tau_\nu^*} \equiv \frac{M_d}{M_p}\frac{1}{\tau_\nu} \qquad (3)$$

is the "mass-reduced viscous rate," which we define in terms of the following quantities: the viscous time $\tau_\nu = \frac{2}{3}r_p^2/\nu(r_p)$ and the proxy disk mass $M_d = 4\pi r_p^2 \Sigma_Z(r_p)$, where $\Sigma_Z = \dot{M}/(3\pi\nu)$ is the surface density profile in the absence of the planet (DLL). For comparison, the type II migration rate for planets less massive than the disk is $-1/\tau_\nu$ (Ward 1997). And for planets more massive than the disk (upon which we focus), type II predicts the rate to be $-(M_d/M_p)^\gamma/\tau_\nu^*$, where γ is a positive number whose value depends on the assumed background disk profile (Syer & Clarke 1995; Ivanov et al. 1999).

Figure 2 (top left panel) shows the migration rates from the simulations. The curves in the top left panel are from DLL, in which we ran simulations with $q \leqslant 10^{-3}$ and $h = 0.05$, and fit

the resulting ΔT to a power-law expression. The extrapolation of those curves to higher q is clearly discrepant with our simulations here.

For our present simulations with higher-mass planets, we see that at high enough q, planets migrate outward. For example, focusing first on the simulation set with $h = 0.05$ (filled diamonds), we see that the subset with $\alpha = 0.01$ transitions to outward migration at $q \gtrsim 4 \times 10^{-3}$. At lower α (and still $h = 0.05$), the transition to outward migration occurs at a lower q.

The transition from inward to outward migration happens alongside another transition: the disk becomes eccentric. In the bottom left panel of Figure 2, we plot the maximum eccentricity in the disk $e_{\max}$ versus q, where the eccentricity is measured by averaging the eccentricity vector within each ring of the disk and then time-averaging the resulting (scalar) eccentricity (Teyssandier & Ogilvie 2017). Comparing each subset of simulations in the top left and bottom left panels, we see that migration is inward in nearly circular disks and outward in eccentric ones (i.e., when $e_{\max} \gtrsim 0.1$).

As seen in Figure 2, both transitions occur above a critical q that depends on α and h. We find empirically that the transition occurs at roughly a fixed value of

$$K' \equiv Kh^2 = \frac{q^2}{\alpha h^3}. \qquad (4)$$

The right panels of Figure 2 replot the data in the left panels, but now with K' on the x-axis. We observe that at $K' \gtrsim 20$, i.e., at

$$q \gtrsim 1.5 \times 10^{-3}\left(\frac{\alpha}{0.001}\right)^{1/2}\left(\frac{h}{0.05}\right)^{3/2}, \qquad (5)$$

the migration rate transitions from inward to outward, and the disk eccentricity transitions from $\lesssim 0.1$ to $\gtrsim 0.2$. The parameter K' has been found empirically to correlate with the width of the gap for planets not massive enough to excite a significant disk eccentricity (Kanagawa et al. 2016; DLL). Kley & Dirksen (2006) and Teyssandier & Ogilvie (2017) found that for $\alpha = 0.004$ and $h = 0.05$, disks become eccentric when $q \gtrsim 3 \times 10^{-3}$, in agreement with Equation (5).

The theory laid out in Lubow et al. (1999) and Teyssandier & Ogilvie (2016, 2017) shows that the disk's eccentricity excitation is sensitive to the density profile, because the density profile controls whether the resonances that excite eccentricity are stronger than those that damp it. Hence, the fact that K'—and hence the gap width—appears to control whether disks are eccentric or not is not too surprising. Nonetheless, although the theory of Teyssandier & Ogilvie (2016) successfully predicts many aspects of their simulations, it does not reproduce the correct threshold for where eccentricity is excited, so they may be missing an effect.

3.2. Why Do Planets Migrate Outward in Eccentric Disks?

Figure 3 shows the steady-state profiles of surface density and eccentricity for simulations that have $h = 0.05$ and K' near the migration transition. In the top row, migration is inward and the disk is nearly circular; in the bottom, migration is outward and the disk is eccentric. The profiles are time-averaged in steady state over 10,000 orbits, which is much longer than the precessional times. As seen in the Σ profiles, higher values of K' systematically result in deeper gaps.
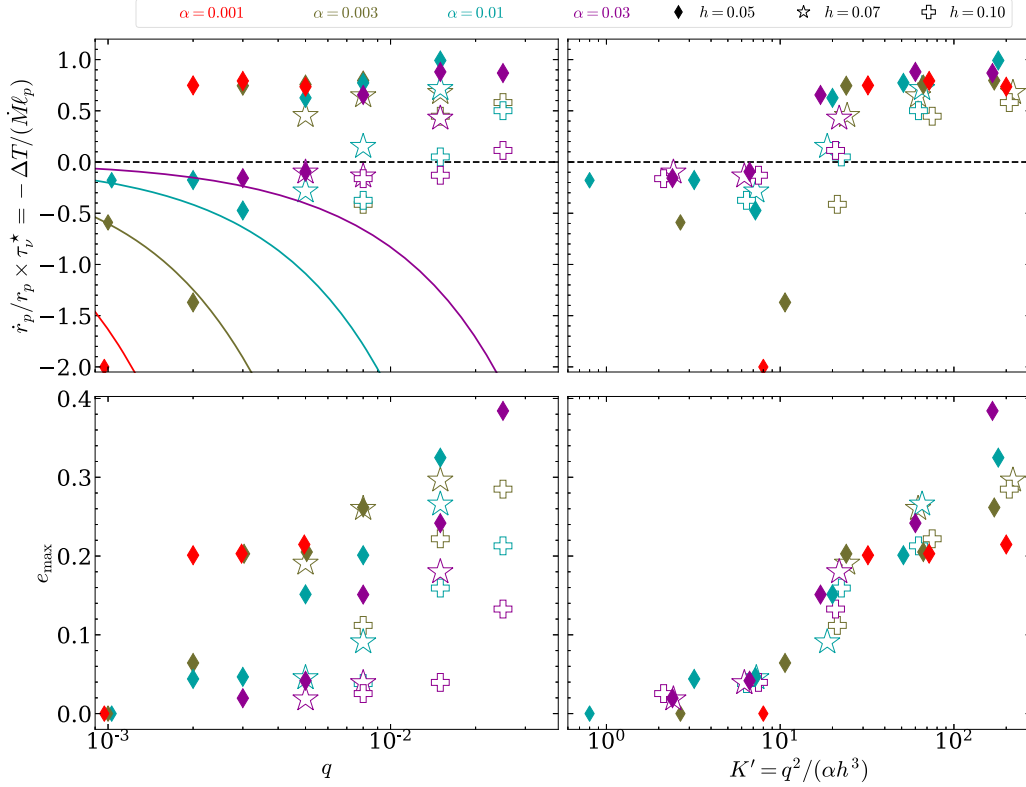
Figure 2. Dependence of the migration rate and maximum disk eccentricity on q and the gap-width scaling parameter K'. The curves in the top left panel summarize the scalings found from DLL for lower-mass ($q \leqslant 10^{-3}$) planets at $h = 0.05$ after extrapolating to these masses. Note that points with $q = 10^{-3}$ are taken from DLL.

In the circular disks, the gaps are nearly symmetric relative to the planet's position, while in the eccentric disks, the outer half of the gap becomes significantly wider than the inner one. In addition, the circular disks have a modest density pileup outside of the planet's orbit, and the eccentric ones have a deficit. The sign and magnitude of the pileup is dictated by the value of ΔT (as shown in Equation (19) of DLL, which follows from Equation (7) below).

Turning to the eccentricity profiles, we see that above the transitional K', it is the outer disk that develops a significant eccentricity. And, although not shown in the figure, the eccentric disks precess coherently,[6] and the amplitude of the eccentricity remains unchanged over multiple viscous times. This points to the eccentricity being a free mode of the disk (Teyssandier & Ogilvie 2016; Lee et al. 2019), with an excitation that balances viscous damping to maintain the mode in a steady state (as in circumbinary disks; see Muñoz & Lithwick 2020).

The right panels show T_{dep}, the cumulative torque deposited into the disk (within each r) by the damping of waves. To calculate T_{dep}, we evaluate the angular momentum flux carried by waves and then remove from that the gravitational torque excited by the planet (DLL). We see that throughout most of the outer disk, T_{dep} increases with r, showing that the torque deposition per unit r is positive there; i.e., that region is responsible for pushing the planet inward. Similarly, most of the inner disk pushes the planet outward, as T_{dep} decreases with

r when $r < r_p$. Far beyond the planet—outside a few $\times r_p$—T_{dep} flattens and approaches ΔT; i.e., all of the torque excited by the planet is eventually deposited in the disk. We henceforth use the T_{dep} profiles to examine what is causing ΔT to become negative in eccentric disks.

Figure 3 shows that the torque on the inner disk is always

$$T_{dep}(r = r_p) \approx -\dot{M}\ell_p. \tag{6}$$

Equation (6) is a generic result for deep gaps in steady-state disks. It follows from the conservation of angular momentum flux, which we approximate here as

$$T_{dep}(r) \approx 3\pi\nu\langle\Sigma\rangle\ell - \dot{M}\ell \tag{7}$$

(see DLL for the full expression). Therefore, if the gap is sufficiently deep, the first term on the right-hand side may be neglected at r_p, confirming Equation (6). In the right panels, we also convert the Σ profiles to T_{dep} via Equation (7). The result is shown as dotted curves. The fact that these agree with the directly calculated T_{dep} confirms that the disk is in viscous steady state.

Given the value of the torque on the inner disk (Equation (6)), it must be that ΔT becomes negative in eccentric disks because the torque on the outer disk weakens. But why? From the theory in Section 1.1, we must examine torque excitation and deposition.

1. Excitation. For a given Σ profile, eccentricity could lower ΔT if it lowers the amplitude of the excited waves in the outer disk and hence lowers the angular momentum carried by them. (We also include in this category the change in co-orbital torques; see below.)

---

[6] For some large q simulations, we find a second bump in the eccentricity profile in the outer disk that has a low amplitude (e.g., the purple curve in the bottom middle panel of Figure 3) and precesses at a different rate than the main bump. But, as seen in the right panel, the torque is unaffected by this secondary mode.
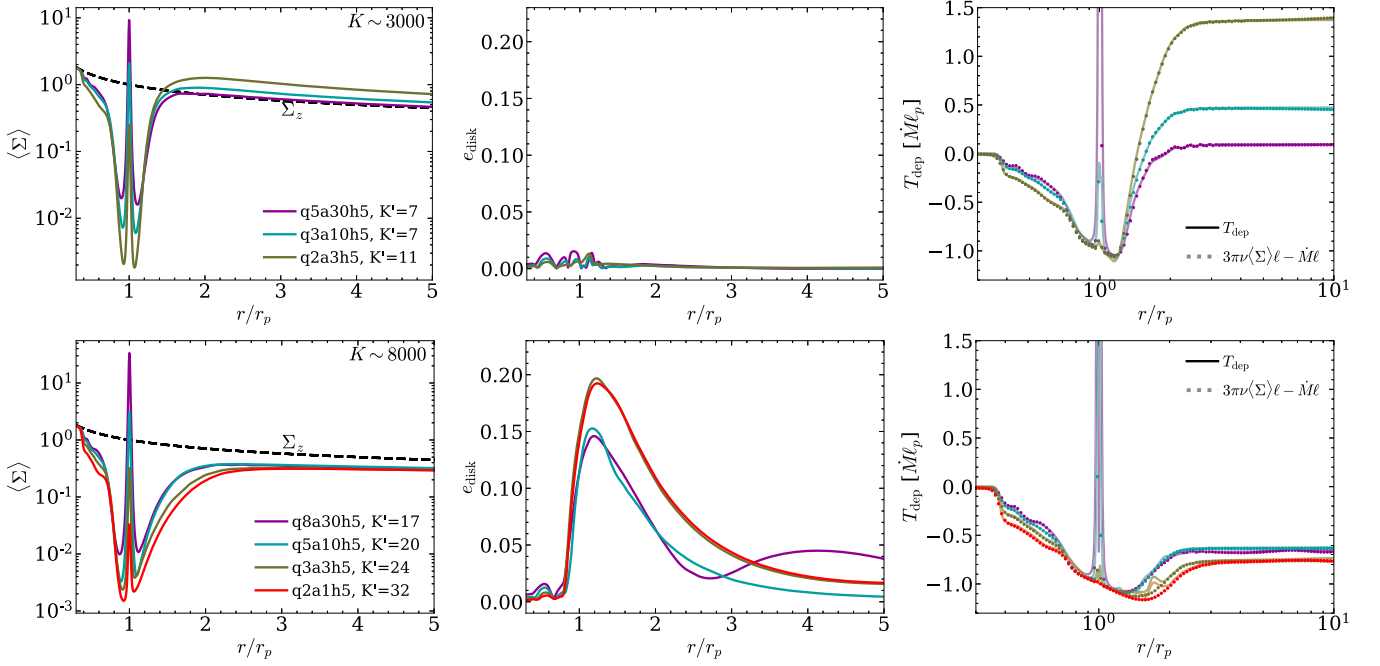
Figure 3. Profiles of surface density, eccentricity, and (cumulative) deposited torque in some nearly circular disks (top panels) and eccentric disks (bottom panels). Each profile is time-averaged over the final 10,000 orbits of the simulation, after the torque has reached its steady-state value. Eccentric disks have more extended outer gaps and weaker outer torques. The latter forces their total torque, $\Delta T \equiv T_{\rm dep}|_{r \gg r_p}$, to be negative. Simulations are labeled such that, e.g., "q8a30h5" corresponds to $q = 8 \times 10^{-3}$, $\alpha = 30 \times 10^{-3}$, and $h = 5 \times 10^{-2}$.

2. Deposition. For a given ΔT, eccentricity could increase the distance waves travel before they damp. A longer damping length means a wider gap (from Equation (7)), which implies that at the location where the waves are excited, Σ is lower, and hence the wave amplitude is lower.

We examine item 1 in Figure 4 by comparing the simulated values of ΔT with a linear calculation of ΔT in a circular disk whose $\Sigma(r)$ profile is the same as that from the simulation[7] (see DLL for our linear calculation method.) We see that for the circular disks ($K' \lesssim 20$), the linear calculation adequately predicts what is found in the simulations. But for the eccentric disks, it overpredicts ΔT. We infer that the disk being eccentric lowers ΔT, as suspected in item 1. A more detailed examination shows that much of the lowering is indeed due to outer waves carrying less angular momentum in the simulated eccentric disk (relative to the linear calculation). But there is an additional effect: the co-orbital torques become stronger (more negative) in the eccentric disks. We find this effect to be subdominant up to $K' \sim 50$; for K' larger than that, the two effects are comparable.

Turning to item 2, the right panels of Figure 3 show that the damping length is indeed longer in the eccentric disks. Unfortunately, we have not been able to quantify the relative importance of items 1 and 2. For a partial quantification of the latter, the curves in Figure 4 show the extrapolations from the circular planet simulations (as in Figure 2). These lie above the open diamonds for the eccentric disks ($K' \gtrsim 10$), and one of the reasons for the discrepancy is that the gap shape for the open diamonds is wider than would be implied in the extrapolations. In truth, explanations 1 and 2 are entangled;
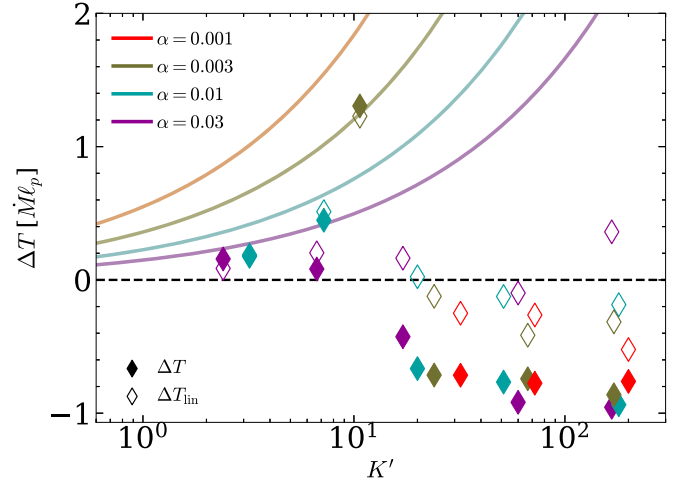

Figure 4. Comparison of ΔT (filled symbols) to the linear ΔT (open symbols) calculated from the $\langle \Sigma \rangle$ profiles for disks with $h = 0.05$. The solid lines show the extrapolations of the circular disk results of DLL to these masses.

e.g., when waves are excited to lower amplitudes, they travel further before becoming nonlinear and damping. But for a first-principles derivation, one must extend the theory of Goodman & Rafikov (2001) to investigate more massive planets and viscous disks.

4. Summary and Discussion

4.1. Summary

Figure 2 encapsulates our main result: planet migration transitions from inward to outward when the planet exceeds around 2 $M_{\rm J}$ for the fiducial values $\alpha = 0.001$ and $h = 0.05$ (Equation (5)). This transition coincides with the disk

---

[7] One could check hypothesis 1 directly by extending the linear theory of torque excitation to an eccentric disk. We defer such an analysis to future work.

becoming eccentric. In Section 3.2, we showed why eccentric disks lead to outward migration.

We find that the total torques are always close in magnitude to the advection torque ($|\Delta T| \sim \dot{M}\ell_p$), whether migration is inward or outward (Figure 2). As a result, the migration rates are comparable in magnitude to the "mass-reduced viscous rate" (Equation (2)).[8] It is not surprising that $|\Delta T| \sim \dot{M}\ell_p$ when migration is outward, because the inner torque is always equal to $-\dot{M}\ell_p$ for deep gaps (Section 3.2); so, if the outer torque is subdominant, the total torque will also be close to $-\dot{M}\ell_p$. But it is surprising that, even when migration is inward, it is never the case that $\Delta T \gg \dot{M}\ell_p$. We speculate that this is because a planet always acts as a leaky sieve, so the pileup beyond the planet can never be too big. That would, in turn, imply that the normalized torque cannot be too large because of the close connection between the pileup and the normalized torque (DLL). But why the planet should always act as a leaky sieve remains an open question.

4.2. Assessment of Key Assumptions

1. α-model. Perhaps our most questionable assumption is that of α-viscosity. If angular momentum is transported by a nonviscous mechanism, such as disk winds, then the gap shapes would be different, and hence so would the torques.
2. Low-mass disk. Fixing the planet's orbit is a good approximation when the planet's migration timescale ($\sim \tau_\nu^*$) is shorter than the gas radial drift timescale (τ_ν) or, equivalently, when $M_d \lesssim M_p$.
3. Circular planet orbit. An eccentric planet will introduce a forced component to the disk eccentricity on top of the free component that is excited above the transitional mass. The planet's eccentricity will also modify the torque on the disk. D'Angelo et al. (2006) included the backreaction of the disk on the planet and found that the planet's eccentricity is rapidly excited, which affects the migration direction. But their inner disks are severely depleted, perhaps due to their inner boundary condition, an insufficient run time compared to the viscous time, or material being lost onto the planet. Moreover, their disks are at least as massive as the planet, invalidating our low-mass disk assumption. In the future, we plan to determine whether the planet's eccentricity is excited or damped in low-mass steady disks, as has been done for stellar binaries (e.g., Muñoz et al. 2019; D'Orazio & Duffell 2021). In the latter case, it has been found that the binary's eccentricity damps if it is below a threshold eccentricity of around 0.1, even though the disk is very eccentric.
4. 2D disk. For high-mass planets, gaps are much wider than the disk scale height, so the 2D treatment should adequately capture the excitation and deposition torques.
5. No accretion onto planet. Our large softening parameter prevented planetary accretion. Realistic modeling of accretion requires high resolution, in addition to a more accurate treatment of the thermal state of the gas, disk self-gravity, and three dimensions (e.g., Fung et al. 2019). If a significant fraction of the disk's radial mass flow ends

up in the planet, the migration rates would change significantly. Additionally, the torque from the circumplanetary region is unrealistic. But we have checked that this torque is small, typically contributing between 0.1 and 0.25 to the dimensionless migration rates in Figure 2.
6. Locally isothermal equation of state. Adopting a finite cooling time, rather than the instantaneous cooling that we assume, would affect the deposition profile. That is because linear waves deposit angular momentum into the disk even in the absence of viscous dissipation, and the amount depends on the cooling time (Miranda & Rafikov 2020). We suspect that this dependence is minimal for the very massive planets considered in this paper, for which viscous dissipation (including by shocks) likely dominates over the aforementioned linear wave deposition.
7. Inner boundary condition. For our results not to depend on the inner boundary, the inner wave-killing zone must be far enough from the planet that most of the torque excitation occurs within the simulation domain (DLL). We have checked that by examining the excitation profile. In addition, we have tested roughly half of our $h < 0.1$ simulations by continuing them in a domain with a smaller wave-killing boundary (down to $0.2r_p$) and found in these cases that the change in torque was small. Note that the $h = 0.1$ simulations require a larger radial domain (see footnote 2) because the wave excitation profile is broader at larger h.

4.3. Comparison to Prior Work

Previous studies have found outward migration of massive planets, but these require either steeply falling surface density profiles (Chen et al. 2020) or extremely massive disks to induce either type III migration (Masset & Papaloizou 2003) or gravitational instability (Lin & Papaloizou 2012; Cloutier & Lin 2013). By contrast, we find outward migration more generally for super-Jupiters, subject to the assumptions listed above.

Recently, Duffell et al. (2020) examined a setup similar to ours and found that ΔT reverses sign in the brown dwarf regime, but for $h = 0.1$ and $\alpha \geqslant 0.03$. Using Equation (5) for their parameters, we find general agreement with their transitional masses (see their Figure 5), suggesting that the torque reversal reported by Duffell et al. (2020) is equivalent to ours.

4.4. Directly Imaged Planets

The $2\,M_J$ threshold that we have uncovered is intriguingly similar to the lowest-mass giant planets discovered via direct-imaging techniques (e.g., Bowler & Nielsen 2018). Due to their large masses and wide separations, these planets were once thought to originate from gravitational instabilities. But recent evidence points to a mass distribution that may be consistent with the core accretion scenario (Nielsen et al. 2019; Wagner et al. 2019). Thus, those super-Jupiters detected via direct imaging could be the outcome of core accretion but followed by outward migration in an eccentric disk. This scenario would not require the presence of additional giants, as would be the case for jointly migrating planets trapped in mean-motion resonance (Crida et al. 2009). It has indeed been speculated that outward migration could explain the properties of directly

---

[8] For comparison, the type II rate, $1/\tau_\nu$, is dramatically slower than the mass-reduced viscous rate when $M_d \ll M_p$. But for $M_d \sim M_p$, the type II rate is close to the true rate in magnitude, even though type II can predict the wrong sign.

imaged planets, e.g., as pointed out recently by Bohn et al. (2021) in the context of their discovery of an $\sim 6\,M_J$ planet at $\gtrsim 115$ au from its star. We propose that such planets could have migrated via interaction with an eccentric disk.

Appendix A
The Indirect Potential

We run our simulations in the stellocentric frame, where the gravitational acceleration for a fluid element located at position $\boldsymbol{r}$ relative to the star is

$$\ddot{\boldsymbol{r}} = -GM_\star \frac{\boldsymbol{r}}{r^3} - GM_p \frac{(\boldsymbol{r} - \boldsymbol{r}_p)}{|\boldsymbol{r} - \boldsymbol{r}_p|^3}$$
$$- GM_p \frac{\boldsymbol{r}_p}{r_p^3} - G \int \frac{\boldsymbol{r}}{r^3} dm, \qquad (A1)$$

where $dm = \Sigma r dr d\phi$ is the mass element of the disk. The first two terms are the direct accelerations due to the star and planet, while the last two terms are the indirect accelerations due to the acceleration of the star by the planet and disk. We neglect the last term in the simulations both because we consider small disk masses and because it is proportional to disk eccentricity and so averages out on the precessional timescale.

We now consider how the indirect terms affect the torque measurements. We will show that the last term in Equation (A1) has a subdominant effect, so we do not include it in our torque measurements in the body of the paper. Equation (A1) is evaluated in the stellocentric frame, but the total torque on the planet–star binary is most easily evaluated in the barycentric frame. In this frame, the disk torques the binary according to

$$\dot{L}_b = \int \left[GM_\star \frac{\boldsymbol{R} \times \boldsymbol{r}}{r^3} + GM_p \frac{\boldsymbol{R} \times (\boldsymbol{r} - \boldsymbol{r}_p)}{|\boldsymbol{r} - \boldsymbol{r}_p|^3} \right] dm, \qquad (A2)$$

where L_b is the angular momentum of the binary and $\boldsymbol{R}$ is the position of a disk element with respect to the star–planet–disk center of mass. Note that the third term of Equation (A1), which is the acceleration of the star due to the planet, does not contribute to $\dot{L}_b$. The stellocentric and barycentric disk positions are related via the center-of-mass position of the star, $\boldsymbol{r} = \boldsymbol{R} - \boldsymbol{R}_\star$, where

$$\boldsymbol{R}_\star = -\mu_p \boldsymbol{r}_p - \mu_d \boldsymbol{r}_d \qquad (A3)$$

and $\mu_{p,d} = M_{p,d}/(M_\star + M_p + M_d)$ are the mass ratios of the planet and disk, $M_d = \int dm$ is the disk mass, and $\boldsymbol{r}_d = \int \boldsymbol{r} dm / M_d$ is the center-of-mass position of the disk. Carrying out the cross products in terms of the stellocentric positions and approximating $\dot{L}_b \approx \dot{L}_p = M_p \ell_p \dot{r}_p / (2r_p)$ for small mass ratios, we find

$$\dot{L}_p \approx GM_p \int \boldsymbol{r} \times \frac{\boldsymbol{r} - \boldsymbol{r}_p}{|\boldsymbol{r} - \boldsymbol{r}_p|^3} dm$$
$$- GM_p \int \boldsymbol{r}_p \times \frac{\boldsymbol{r}}{r^3} dm$$
$$- GM_d \int \boldsymbol{r}_d \times \left[\frac{\boldsymbol{r}}{r^3} + q \frac{\boldsymbol{r} - \boldsymbol{r}_p}{|\boldsymbol{r} - \boldsymbol{r}_p|^3} \right] dm. \qquad (A4)$$

The first line is the familiar torque of the disk on the planet due to the direct acceleration (second term of Equation (A1)). The second and third lines are corrections arising from the displaced disk center of mass (the last term in Equation (A1)). We neglect the contribution from the third line, as we find that $\boldsymbol{r}_d$ in all simulations is on the order of $e_{\max} r_p$, making the third line an order $e_{\max} M_d / M_p \ll 1$ correction. The remaining correction to the direct torque is the second line, which we measure, a posteriori, to be $\lesssim 0.2 \dot{M} \ell_p$. If we were to include this term in the ΔT values shown in Figure 2 (which only contain the direct torque), the points at $K \gtrsim 20$ would shift by a minor amount, but not enough to affect our main conclusions.

Appendix B
Barycentric Outer Boundary Condition

We apply the inflow boundary condition of DLL at the disk's outer boundary. The distant inward flow is assumed to be axisymmetric around the star–planet barycenter, which is displaced from the origin of the simulation. We prescribe the inflow rate, $\dot{M}$, and set $\Sigma = \dot{M}/(3\pi\nu)$ at the boundary. The fluid velocities are set to their barycentric values, $v_{r,\text{bary}} = \dot{M}/(-2\pi r_b \Sigma)$, where r_b is the distance to the barycenter, and $v_{\phi,\text{bary}}$ is the pressure-corrected Keplerian velocity. We then transform the barycentric velocities to FARGO3D's stellocentric rotating frame using

$$\begin{pmatrix} v_r \\ v_\phi \end{pmatrix} = \begin{pmatrix} \cos(\phi_b - \phi) & -\sin(\phi_b - \phi) \\ \sin(\phi_b - \phi) & \cos(\phi_b - \phi) \end{pmatrix} \begin{pmatrix} v_{r,\text{bary}} \\ v_{\phi,\text{bary}} - nr_b \end{pmatrix}, \quad (B1)$$

where $n = \sqrt{1 + q}\, \Omega_p$ is the planet's mean motion, and ϕ_b is the azimuthal angle in the barycentric coordinate system. For each cell along the stellocentric boundary with Cartesian stellocentric coordinates (x, y), we first compute $r_b = \sqrt{(x - \mu r_p)^2 + y^2}$, where $\mu = q/(1 + q)$, and then apply the transformation given by Equation (B1) with

$$\cos(\phi_b - \phi) = \frac{r}{r_b}\left(1 - \frac{\mu r_p}{r}\right),$$
$$\sin(\phi_b - \phi) = \frac{\mu r_p}{r_b}. \qquad (B2)$$

Teyssandier & Ogilvie (2017) used a boundary condition similar to Equation (B1) but with $v_{r,\text{bary}} = 0$.
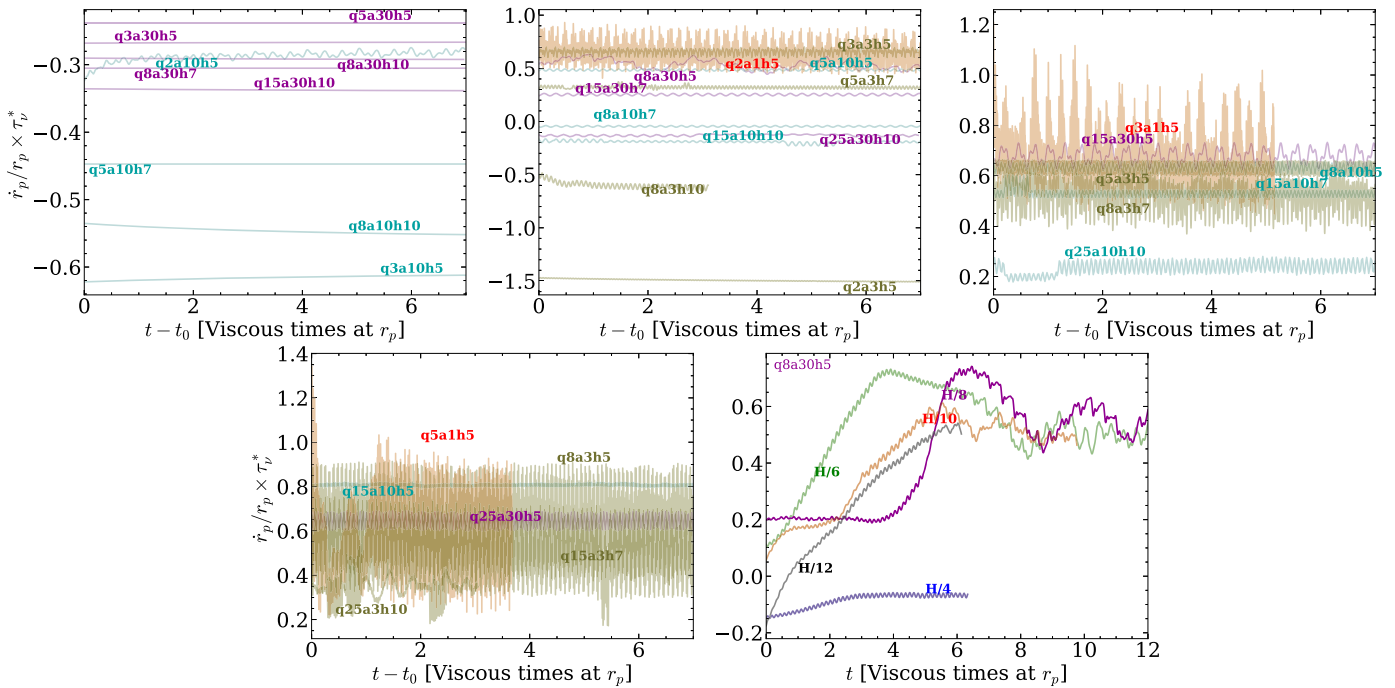
Figure 5. Convergence of migration rates with time (first four panels) and with resolution for one example simulation (fifth panel). In the first four panels, we show only the final seven viscous times, while in the fifth panel, we show the first 12 viscous times. For each simulation, we time-average each point over 1000 orbits to remove short-timescale variations. See the caption of Figure 3 for our naming convention.

Appendix C
Convergence of Simulations

We run each simulation in two stages. In the first stage, we start the simulation with the steady-state planetless solution, fix $\dot{M}$ at both boundaries, and evolve the disk long enough for the gap to open and reach a quasi-steady state. During the second stage, we switch to the inner boundary condition described in Section 2.1 that allows $\dot{M}$ at the inner boundary to adjust as the disk evolves to a global steady state.

Simulations reach a steady state once the time- and azimuthally averaged $\dot{M}$ is independent of r. For our lowest α, we find that the average $\dot{M}$ in the outer disk ($r > 1.05r_p$) is within 10% of the average inner disk $\dot{M}$ ($r < 1.05r_p$). These $\dot{M}$ typically agree to less than 1% in the larger α cases.

In the first four panels of Figure 5, we show that all of our migration rates are converged in time. Each point is normalized to the current value of $\dot{M}$ at the inner boundary and time-averaged over a window of 1000 orbits to remove short-timescale oscillations. For clarity, we only show the final seven viscous times, but we note that many of the simulations are converged in the first few viscous times.

The fifth panel of Figure 5 shows the dependence of ΔT on the simulation resolution for one exemplary simulation with $q = 0.008$, $\alpha = 0.03$, and $h = 0.05$. We find that once the resolution exceeds six points per scale height, the migration rate is converged. Moreover, we showed in DLL with many more simulations that our fiducial resolution of eight points per scale height was adequate for determining ΔT.

As discussed in Section 2.1, some simulations use a smaller inner boundary in order to capture all of the torque excited by the planet. The amount of missing torque is typically small for simulations with $h < 0.1$ that have an inner boundary at $0.3r_p$. The only exception to this is the q8a30h5 simulation, for which moving the inner boundary to $0.1r_p$ lowered the migration rate

by ~50%. This reduction was due to an ~50% smaller disk eccentricity, which resulted in a comparatively larger outer disk torque. Nonetheless, this simulation was on the boundary between low and high eccentricity (see Figure 2) and therefore does not affect the transitional K' that we find.

ORCID iDs

Adam M. Dempsey ⓘ https://orcid.org/0000-0001-8291-2625
Diego J. Muñoz ⓘ https://orcid.org/0000-0003-2186-234X
Yoram Lithwick ⓘ https://orcid.org/0000-0003-4450-0528

References

Armitage, P. J. 2010, in Astrophysics of Planet Formation, ed. Philip J. Armitage (Cambridge: Cambridge Univ. Press), 2010
Artymowicz, P. 1993, ApJ, 419, 166
Benítez-Llambay, P., & Masset, F. S. 2016, ApJS, 223, 11
Bohn, A. J., Ginski, C., Kenworthy, M. A., et al. 2021, A&A, 648, A73
Bowler, B. P., & Nielsen, E. L. 2018, Handbook of Exoplanets (Berlin: Springer), 155
Chen, Y.-X., Zhang, X., Li, Y.-P., Li, H., & Lin, D. N. C. 2020, ApJ, 900, 44
Cloutier, R., & Lin, M.-K. 2013, MNRAS, 434, 621
Crida, A., Masset, F., & Morbidelli, A. 2009, ApJL, 705, L148
Crida, A., Morbidelli, A., & Masset, F. 2006, Icar, 181, 587
D'Angelo, G., Lubow, S. H., & Bate, M. R. 2006, ApJ, 652, 1698
Dempsey, A. M., Lee, W.-K., & Lithwick, Y. 2020a, ApJ, 891, 108
Dempsey, A. M., Muñoz, D., & Lithwick, Y. 2020b, ApJL, 892, L29
D'Orazio, D. J., & Duffell, P. C. 2021, ApJL, 914, L21
Duffell, P. C. 2015, ApJL, 807, L11
Duffell, P. C., D'Orazio, D., Derdzinski, A., et al. 2020, ApJ, 901, 25
Duffell, P. C., Haiman, Z., MacFadyen, A. I., D'Orazio, D. J., & Farris, B. D. 2014, ApJL, 792, L10
Duffell, P. C., & MacFadyen, A. I. 2013, ApJ, 769, 41
Dürmann, C., & Kley, W. 2015, A&A, 574, A52
Fung, J., Shi, J.-M., & Chiang, E. 2014, ApJ, 782, 88
Fung, J., Zhu, Z., & Chiang, E. 2019, ApJ, 887, 152
Ginzburg, S., & Sari, R. 2018, MNRAS, 479, 1986
Goldreich, P., & Tremaine, S. 1979, ApJ, 233, 857
Goldreich, P., & Tremaine, S. 1980, ApJ, 241, 425

Goodman, J., & Rafikov, R. R. 2001, ApJ, 552, 793
Ivanov, P. B., Papaloizou, J. C. B., & Polnarev, A. G. 1999, MNRAS, 307, 79
Kanagawa, K. D., Muto, T., Tanaka, H., et al. 2016, PASJ, 68, 43
Kanagawa, K. D., Tanaka, H., Muto, T., & Tanigawa, T. 2017, PASJ, 69, 97
Kanagawa, K. D., Tanaka, H., Muto, T., Tanigawa, T., & Takeuchi, T. 2015, MNRAS, 448, 994
Kanagawa, K. D., Tanaka, H., & Szuszkiewicz, E. 2018, ApJ, 861, 140
Kanagawa, K. D., & Tanaka, H. 2020, MNRAS, 494, 3449
Kley, W., & Dirksen, G. 2006, A&A, 447, 369
Kley, W., & Nelson, R. P. 2012, ARA&A, 50, 211
Lee, W.-K., Dempsey, A. M., & Lithwick, Y. 2019, ApJL, 882, L11
Lin, D. N. C., & Papaloizou, J. 1986, ApJ, 309, 846
Lin, M.-K., & Papaloizou, J. C. B. 2012, MNRAS, 421, 780
Lubow, S. H., Seibert, M., & Artymowicz, P. 1999, ApJ, 526, 1001
Lunine, J. I., & Stevenson, D. J. 1982, Icar, 52, 14
Masset, F. S., & Papaloizou, J. C. B. 2003, ApJ, 588, 494
Miranda, R., & Rafikov, R. R. 2020, ApJ, 892, 65
Moody, M. S. L., Shi, J.-M., & Stone, J. M. 2019, ApJ, 875, 66

Muñoz, D. J., Lai, D., Kratter, K., & Miranda, R. 2020, ApJ, 889, 114
Muñoz, D. J., & Lithwick, Y. 2020, ApJ, 905, 106
Muñoz, D. J., Miranda, R., & Lai, D. 2019, ApJ, 871, 84
Nielsen, E. L., De Rosa, R. J., Macintosh, B., et al. 2019, AJ, 158, 13
Rafikov, R. R. 2002, ApJ, 572, 566
Regály, Z., Sándor, Z., Dullemond, C. P., & van Boekel, R. 2010, A&A, 523, A69
Robert, C. M. T., Crida, A., Lega, E., Méheut, H., & Morbidelli, A. 2018, A&A, 617, A98
Scardoni, C. E., Rosotti, G. P., Lodato, G., & Clarke, C. J. 2020, MNRAS, 492, 1318
Shakura, N. I., & Sunyaev, R. A. 1973, A&A, 500, 33
Syer, D., & Clarke, C. J. 1995, MNRAS, 277, 758
Teyssandier, J., & Ogilvie, G. I. 2016, MNRAS, 458, 3221
Teyssandier, J., & Ogilvie, G. I. 2017, MNRAS, 467, 4577
Wagner, K., Apai, D., & Kratter, K. M. 2019, ApJ, 877, 46
Ward, W. R. 1997, Icar, 126, 261